Synthesis and spectral characterization of chalcone dervived from 6-Acetyl-2H-1,4-benzoxazin-(4H)-3-one: single-crystal XRD, Hirshfeld surface analysis and DFT calculations.

ABSTRACT

Organic Compound (E)- 6-(3-(p-tolyl)acryloyl)- 2H-benzo[b][1,4]oxazin-3(4H)- one [6TABO] with molecular formula $C_{18}H_{15}NO_3$ was incorporated utilizing Claisen-Schmidt condensation technique. FT-IR and ^{1}H NMR spectra were recorded to recognize the different utilitarian gatherings present in the compound and affirm the synthetic construction. The UV-Visible range study uncovers that the visible is straightforward in the whole apparent locale and the retention is seen at 325.40 nm. Single-crystal XRD concentrates on show that the compound takes shape in the monoclinic framework with a space bunch P 1 21/c 1. The corresponding lattice parameters of the crystal are a = 13.0723 (7) Å, b = 7.1789 (4) Å, c = 16.1812 (9) Å, α=900, β = 109.148 (2)0, γ = 900.

Keywords: Chalcones, Single crystals, Hirshfeld surface, Fingerprint plots, DFT studies.

INTRODUCTION

Chalcones are α,β-unsaturated ketones including the responsive keto-ethylenic bunch (CO-CH=CH-) which gave shaded compounds because of the presence of (CO-CH=CH) the chromophore bunch [1-5].Molecular Hirshfeld surface [6, 7] investigation in the gem portrays a strategy to concentrate on the idea of the intermolecular associations utilizing a dividing of gem space in an inventive visual way. The related unique mark plots [8] address the intermolecular association in an advantageous shading plot.

The present study focused on synthesis of titled compound and single crystal XRD studies. The Hirshfeld surface and 2D fingerprint analyses were performed to study the nature of interactions and their quantitative contributions towards the crystal packing. Structure determination was optimized by Density Functional Theory (DFT) using B3LYP/6-311G++(d, p) method in the ground state.

METHOD

Instruments

Only notable absorption values were included in the IR spectrum, which was acquired in an AVATAR-330 FT-IR spectrophotometer. Using $CDCl_3$ as a solvent and TMS as an internal standard, ^{1}H NMR spectra were acquired at 300 and 400 MHz on Bruker AMX 300 and 400

MHz spectrophotometers. TLC was used to evaluate the reactions and the purity of the products. All melting points were measured in open capillaries and were unadjusted.

Synthesis

6-Acetyl-2H-1,4-benzoxazin-(4H)-3-one (0.4716g) and 4-methylbenzaldehyde (0.7642g) were mixed in an ethanolic solution for 4 hours with a little amount of N/10 sodium hydroxide solution. The resultant solution was placed into ice water and filtered. Ethanol was used to recrystallize the crude Chalcone.

Reaction

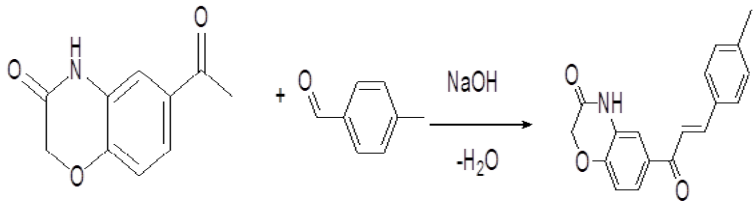

Table 1

Compound	Molecular formula	Molecular weight	Melting point(^{0}C)
6TABO	$C_{18}H_{17}NO_3$	295.3	148.9

RESULTS AND DISCUSSION

ANALYSIS OF FT-IR SPECTRUM

Infrared spectroscopy provides information on molecular vibration or more accurately, transitions between vibrational and rotational energy levels. The stimulation of bond deformations either stretching or bending, occurs when infrared radiation is absorbed. Various stretching and bending vibrations occur at quantized frequencies. Energy is absorbed and the amplitude of the vibration is increased when infrared light of that frequency is incident on the molecule. When the frequency of molecular vibration matches the frequency of absorbed infrared radiation, the infrared spectrum is obtained. The vibration frequency is determined by the force constant and the atom's decreased mass. Mesomeric effect, inductive effect, field-effect, steric effect, and hydrogen bonding, among other things, alter vibration frequencies when minor modifications in molecular structure are made. The delocalization of the electrons of both unsaturated groups occurs when the carbonyl group conjugates with the double bond/aromatic ring, reducing the double bond character of carbonyl frequency. The resonance is responsible for the lower absorption frequencies of both the >C=C and >C=O groups as illustrated below:

The vibrational frequency of the double bond in conjugation with the carbonyl group is reduced to 1646 cm-1, while the C=C stretching frequency is reduced to 1610 cm-1. The aromatic skeletal stretching causes absorption bands to appear at 1560, 1509, and 1485 cm-^{1}.

The oxazinyl N-H is responsible for the structural frequency of 3234 cm-1. At 1686 cm-^{1}, the amide C=O group of the benzooxazinyl molecule emerges (Fig-1).

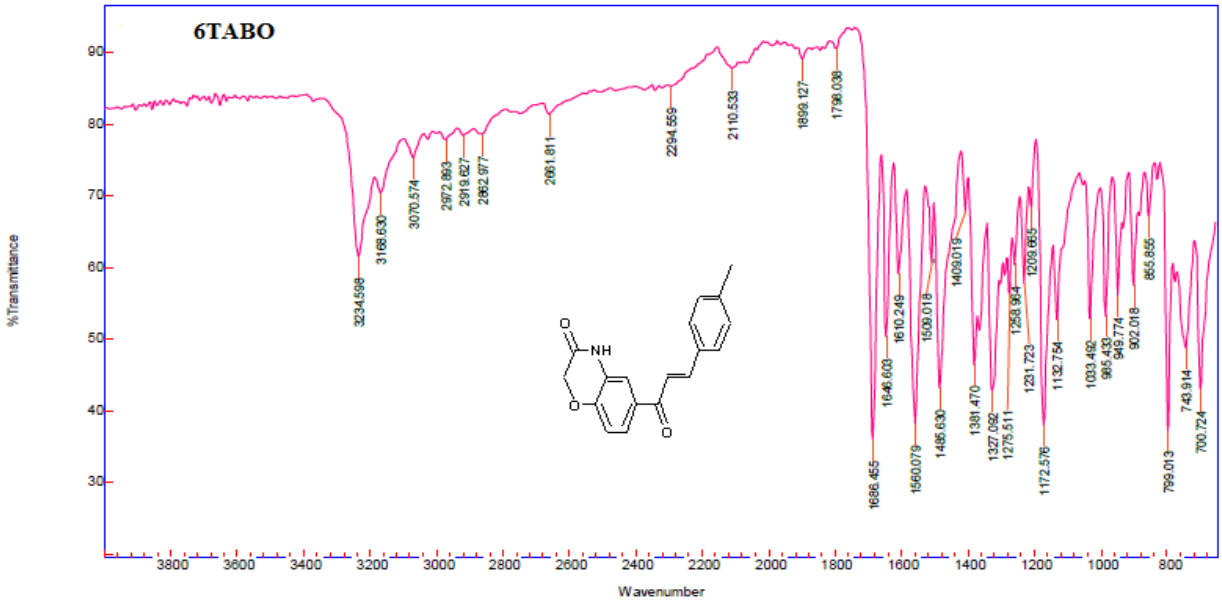

Fig-1. FT-IR Spectrum of compound 6TABO

^{1}H NMR SPECTRA

In recent days, there has been a lot of attention in the literature to correlate proton chemical shifts with substituent constants in diverse systems. Leterbur[11] measured “the 1H NMR spectrum of unsaturated carbonyl compounds of the type RC6H4-CH=CH-CO-CMe3 and looked for Hammett correlations for the ethylenic protons.” Dhami and Stothers[9,10] studied “the ^{1}H NMR spectrum of a large number of acetophenones and styrenes in order to establish the validity of the additivity of substitute Due to the magnetic anisotrophic effect, signals for aromatic protons present in a molecule often arise in the downfield area of roughly 7 ppm. In most of the cases since the absorption of the olefinic protons in the chalcones are also in the aromatic region, it is quite difficult to differentiate the olefinic proton signals from that of the aryl protons.”

In general, the olefinic proton closest to the aromatic ring (H proton) resonates in the deshielding region more than the -proton (H) because it will experience a magnetic field from the induced circulation of electrons in the aromatic ring, augmenting the applied field and thus leading to a higher value.

The ethylenic proton signals in the chemical under investigation are assigned. The ethylenic proton signal is a doublet that is highly isolated from the aromatic proton signals.

The chemical 6TABO has a Hβ proton shift of 7.753 ppm, and the H proton resonates at 6.988 ppm. The protons in the oxazinyl methane group are responsible for the peak at 4.654 ppm. The >NH proton will be allocated to the singlet at 8.082 ppm. The methyl protons at the p-position of the phenyl ring cause the singlet in the up field region (2.332 ppm). (Fig-2).

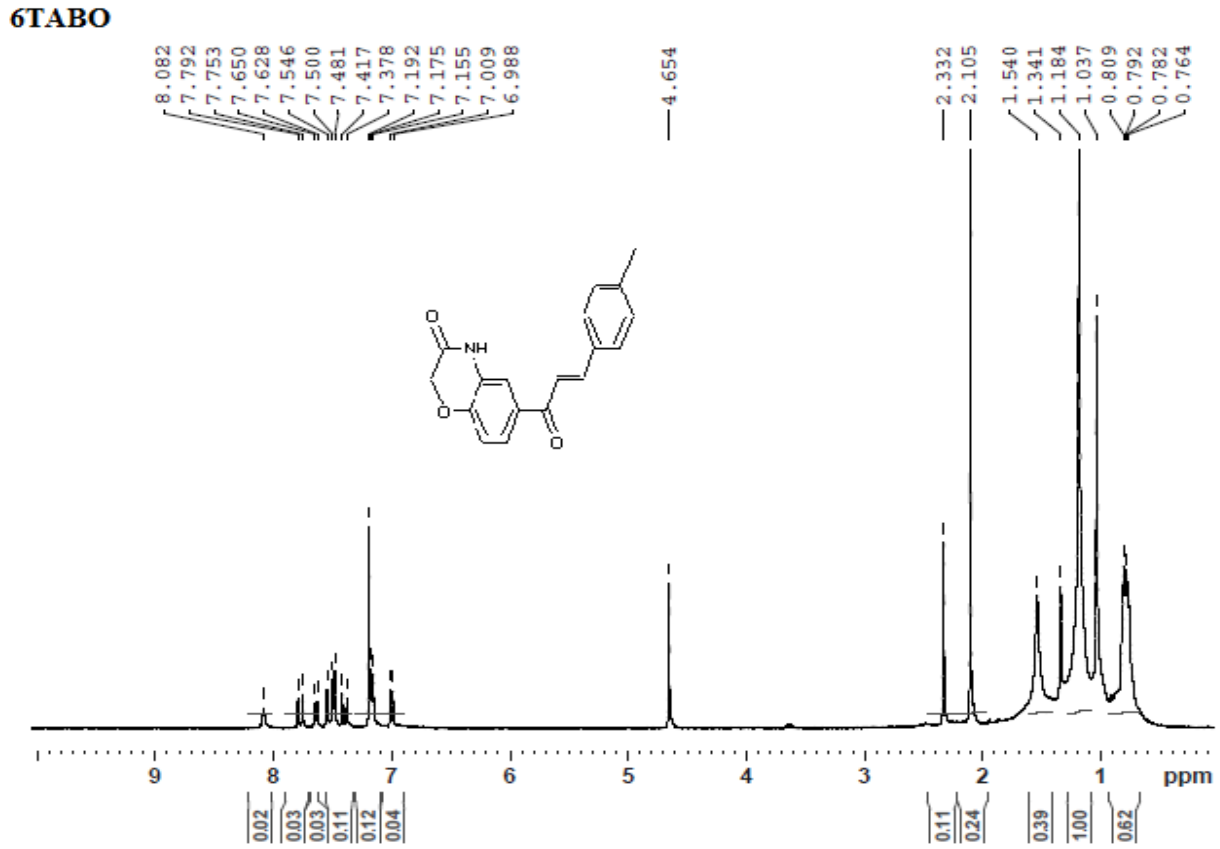

Fig-2.^{1}H NMR Spectrum of compound 6TABO

UV ABSORPTION SPECTRUM

Figure 3 shows the newly synthesized compound UV spectrum that was recorded. The majority of organic compound absorption spectroscopy is based on transitions of n electrons to the π*excited state, which occurs in the 200–700 nm range. In this case, the maximum absorption peak at 325.40 nm (Fig. 3) can be attributed to the n → π* transition and the excitation of the aromatic ring and the C=O group [29].

Table 2

UV spectral data of compound 6TABO

Solvent	λ_{max}	γ_{abs} cm^{-1}
CCl_4	325.40	1.196

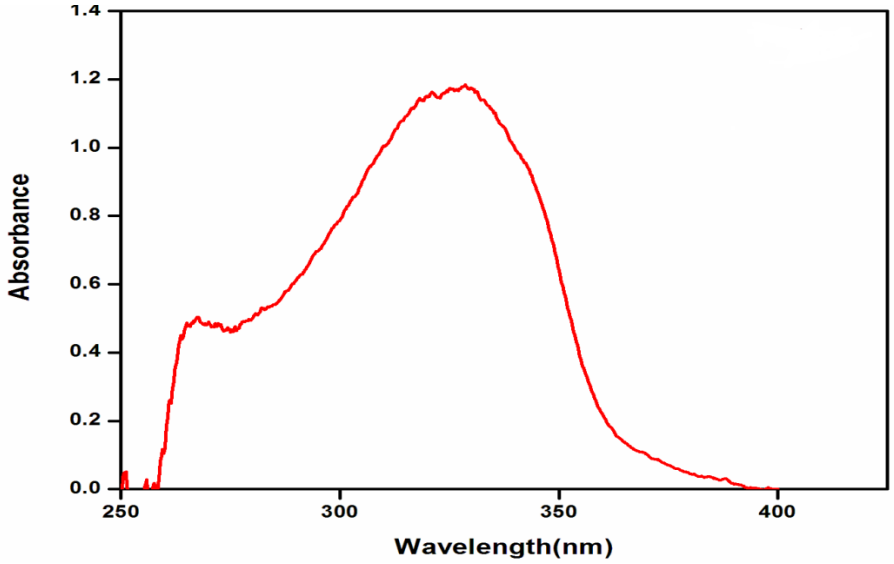

Fig-3.The UV absorption spectrum of compound 6TABO in CCl_4

X-ray crystallographic analysis of compound 6TABO

Spectral investigations and single-crystal X-ray analyses are used to describe the molecule (6TABO). With the following unit cell characteristics, the molecule crystallises in the monoclinic space group P 1 21/c 1: = 900, = 109.148 (2)0, = 900, a = 13.0723 (7), b = 7.1789 (4), c = 16.1812 (9) Direct methods were used to solve the crystal structure using single-crystal X-ray diffraction data taken at 302 (2) K, and full-matrix least-squares approaches were used to refine the structure to a final R-value of 0.0645 for 0.1794 observed reflections. Figures 4 and 5 show the crystal structure of ORTEP and the packing diagram. Table 3 presents crystal data and details of the structure determination for the complex 6TABO, whereas Table 4-6 shows selected bond lengths (), bond angles (0), and Torsion angles (0) for the compound 39.

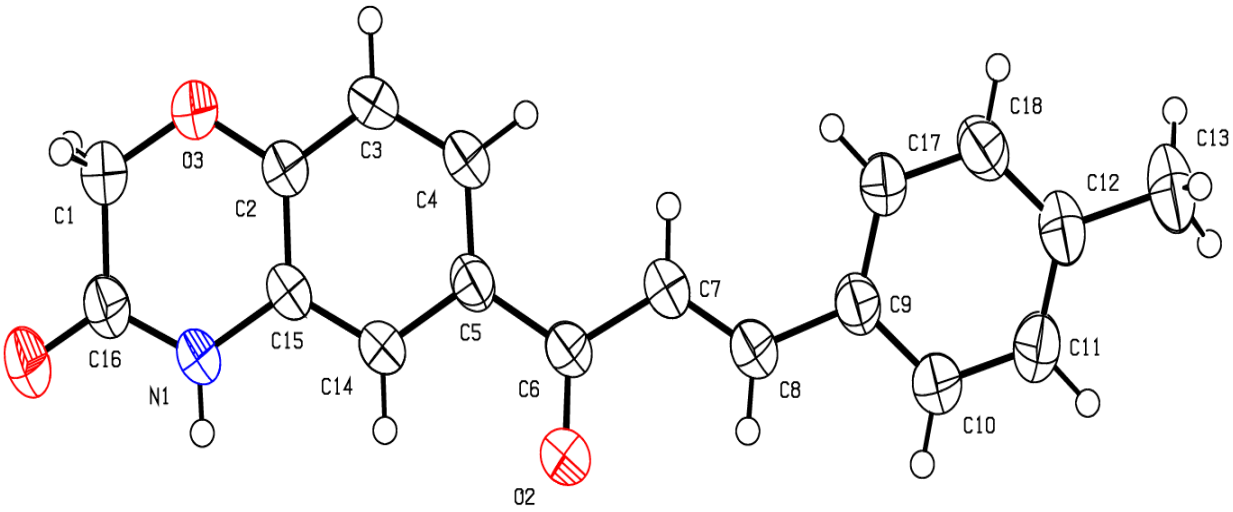

Fig-4. ORTEP structure of compound 6TABO

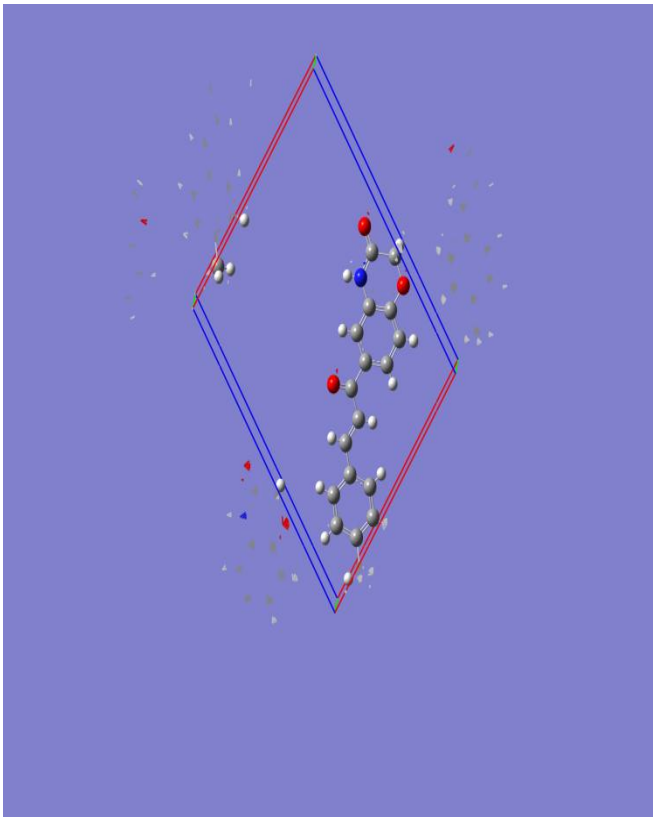

Fig-5. Packing diagram of compound 6TABO

Table-3: Crystal data and details of the structure determination of the compound 6TABO

Empirical Formula	$C_{18}H_{15}NO_3$
Formula weight	293.31 g/mol
Crystal system	monoclinic
Space group	P 1 21/c 1
Cell constant	-
a (Å)	13.0723(7)
b (Å)	7.1789(4)
C (Å)	16.1812(9)
α (Å)	90°
β (Å)	109.148(2)°
γ (Å)	90°
Volume ($Å^3$)	1434.51(14)
z	4
Crystal size (mm)	0.210x 0.290x 0.350
Radiation	**Mo Ka λ** =0.71073Å
Temperature Θ limits (°) Index range	302(2) K 2.67 to 30.11^0 -18<= h <= 18, -10<= k <= 10, -22<= 1 <= 22,
Reflections collected	21206
Goodness-of-fit	1.222
Completeness	99.2%

Table-4: Selected bond lengths (Å) of the compound 6TABO

Bond Lengths			
O1-C16	1.223(2)	02-C6	1.233(2)
03-C2	1.362(2)	O3-C1	1.390(2)
N1-C16	1.334(2)	N1-C15	1.4005(19)
N1-H1A	0.86	C1-C16	1.501(3)
C1-H3	0.97	C1-H1	0.97
C2-C3	1.376(2)	C2-C15	1.385(2)
C3-C4	1.382(3)	C3-H4	0.93
C4-C5	1.387(3)	C4-H5	0.93
C5-C14	1.398(2)	C5-C6	1.475(2)
C6-C7	1.467(2)	C7-C8	1.328(3)
C7-H7	0.93	C8-C9	1.458(2)
C8-H8	0.93	C9-C10	1.384(3)
C9-C17	1.389(3)	C10-C11	1`374(2)
C10-H11	0.93	C11-C12	1.381(3)
C11-H10	0.93	C12-C18	1.38493
C12-C13	1.504(2)	C13-H12	0.96
C13-H2	0.96	C13-H13	0.96
C14-C15	1.37892)	C14-H6	0.93
C17-C18	1.374(2)	C17-H14	0.93
C18-H9	0.93		

Table-5: Selected bond Angles (°) of the compound 6TABO

Bond Angles			
C2-O3-C1	120.12(15)	C16-N1-C15	123.35(16)
C16-N1-H1A	118.3	C15-N1-H1A	118.3
O3-C1-C16	119.58(16)	O3-C1-H3	107.4
C16-C1-H3	107.4	O3-C1-H1	107.4
C16-C1-H1	107.4	H3-C1-H1	107
O3-C2-C3	118.29(17)	O3-C2-C15	121.10(15)
C3-C2-C15	120.61(17)	C2-C3-C4	119.81(17)
C2-C3-H4	120.1	C4-C3-H4	120.1
C3-C4-C5	120.88(16)	C3-C4-H5	119.6
C5-C4-H5	119.6	C4-C5-C14	118.26(16)
C4-C5-C6	123.90(15)	C14-C5-C6	117.82(16)
O2-C6-C7	120.43916)	O2-C6-C5	119.11(15)
C7-C6-C5	120.46(16)	C8-C7-C6	121.13(18)
C8-C7-H7	119.4	C6-C7-H7	119.4
C7-C8-C9	128.62(19)	C7-C8-H8	115.7
C9-C8-H8	115.7	C10-C9-C17	116.96(17)
C10-C9-C8	119.10(17)	C17-C9-C8	123.94(18)
C11-C10-C9	121.97(18)	C17-C10-H11	119
C9-C10-H11	119	C10-C11-C12	120.98(19)
C10-C11-H10	119.5	C12-C11-H10	119.5
C11-C12-C18	117.30917)	C11-C12-C13	120.9(2)
C18-C12-C13	121.84(19)	C12-C13-H12	109.5
C12-C13-H2	109.5	H12-C13-H2	109.5
C12-C13-H13	109.5	H12-C13-H13	109.5
H2-C13-H13	109.5	C15-C14-C5	121.19(16)
C15-C14-H6	119.4	C5-C14-H6	119.4
C14-C15-C2	119.23(15)	C14-C15-N1	121.28(16)
C2-C15-N1	119.49(16)	O1-C16-N1	123.91(18)
O1-C16-C1	119.76(17)	N1-C16-C1	116.32(16)
C18-C17-C9	120.94(18)	O18-C17-H14	119.5
C9-C17-H14	119.5	C17-C18-C12	121.82(180
C17-C18-H9	119.1	C12-C18-H9	119.1

Table-6: Torsion angles (°) of the compound 6TABO

C2-O3-C1-C16	-0.6(3)	C1-O3-C2-C3	178.0(2)
C1-O3-C2-C15	-1.1(3)	O3-C2-C3-C4	179.60(18)
C15-C2-C3-C4	-1.3(3)	C2-C3-C4-C5	-0.3(3)
C3-C4-C5-C14	1.2(3)	C3-C4-C5-C6	-177.22(18)
C4-C5-C6-O2	167.02(19)	C14-C5-C6-O2	-11.4(3)
C4-C5-C6-C7	-12.9(3)	C14-C5-C6-C7	168.72(15)
O2-C6-C7-C8	6.8(3)	C5-C6-C7-C8	-173.29(16)
C6-C7-C8-C9	-179.58(16)	C7-C8-C9-C10	-170.64(19)
C7-C8-C9-C17	9.5(3)	C17-C9-C10-C11	0.7(3)
C8-C9-C10-C11	-179.12(18)	C9-C10-C11-C12	0.9(3)
C10-C11-C12-C18	-1.4(3)	C10-C11-C12-C13	178.52(18)
C4-C5-C14-C15	-0.6(3)	C6-C5-C14-C15	177.95(16)
C5-C14-C15-C2	-1.0(3)	C5-C14-C15-N1	178.83(15)
O3-C2-C15-C14	-179.00(17)	C3-C2-C15-C14	1.9(3)
O3-C2-C15-N1	1.2(3)	C3-C2-C15-N1	-177.92(17)
C16-N1-C15-C14	-179.22(17)	C16-N1-C15-C2	0.6(3)
C15-N1-C16-O1	178.83(16)	C15-N1-C16-C1	-2.1(3)
O3-C1-C16-O1	-178.8(2)	O3-C1-C16-N1	2.1(3)
C10-C9-C17-C18	-1.7(3)	C8-C9-C17-C18	178.10(17)
C9-C17-C18-C12	1.2(3)	C11-C12-C18-C17	0.4(3)
C13-C12-C18-C17	-179.55(18)		

Frontier molecular orbitals and molecular electrostatic potential

FMO investigations have been found to be quite good at predicting the chemical stability of the compounds under study [12]. “Quantum orbitals such as the lowest unoccupied molecular orbital (LUMO) and the highest occupied molecule orbital (HOMO) are extremely essential. LUMO usually refers to the ability to accept an electron, whereas HOMO refers to the ability to donate electrons” [13]. “The HOMO-LUMO energy gap is a crucial statistic for forecasting a molecule's chemical reactivity and dynamic

stability" [14]. "Furthermore, the prediction of the energy difference between FMOs is an excellent indicator for a number of critical characteristics, including chemical hardness (), global softness (S), and polarizability (). Low energy gap of the FMO, as well as strong polarizability, are well-known features of excellent NLO compounds" [15]. The FMO energy gap and global softness (S) were affected by the length and conformation of the alkoxy chain, as shown in Fig. 6 and the ground state isodensity surface plots for the FMOs of 6TABO in Table 7. The FMO energy gap and global softness (S) were affected by the length and conformation of the alkoxy chain, as shown in Table 7. The global softness and polarizability grow as the length of terminal wings increases. As a result, it is expected that as the length of the alkoxy chains increases, their properties would improve, making them more suitable for nonlinear optical applications, as shown in Table 7.

Compound 6TABO				
Dipole Moment		**5.9703**		
HOMO	**LUMO**	**ΔE (E_{LUMO}-E_{HOMO})**	**η = ΔE(E_{LUMO}-E_{HOMO})/2**	**S = 1/ΔE = (1/2η)**
E_{HOMO} (a.u) -0.23701	**E_{LUMO} (a.u)** -0.09593	0.14108	0.07054	7.088177
E_{HOMO-1} (a.u) -0.24516	**E_{LUMO+1} (a.u)** -0.04890	0.19626	0.09813	5.095282
E_{HOMO-2} (a.u) -.026224	**E_{LUMO+2} (a.u)** -0.03780	0.22444	0.11222	4.455534
E_{HOMO-3} (a.u) -0.26304	**E_{LUMO+3} (a.u)** -0.3144	0.2316	0.1158	4.317789

Table-7.Molecular orbital energies, hardness (η), and global softness (S) of 6TABO

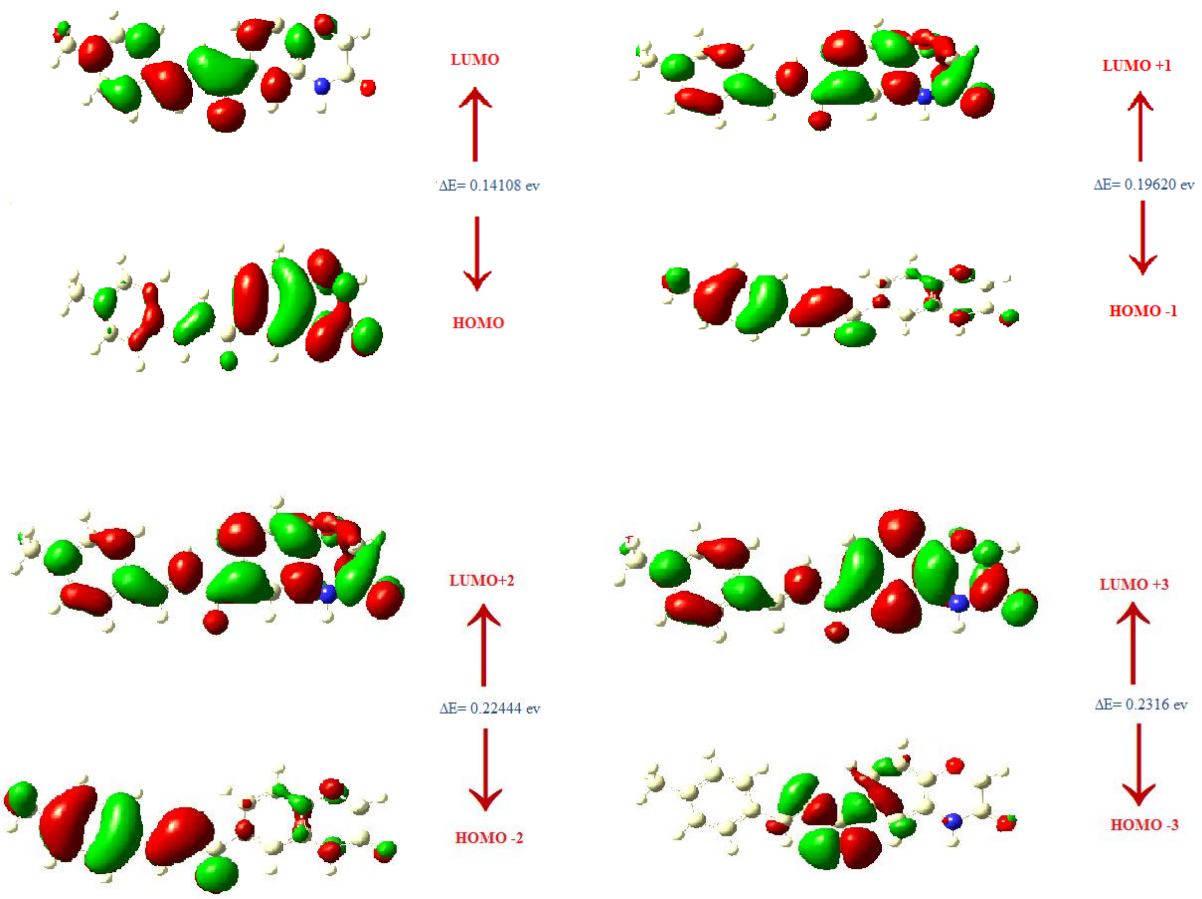

Fig. 6. The calculated ground state isodensity surface plots for frontier molecular orbitals of 6TABO

Mulliken charges distribution

Mulliken obtains the natural population analysis of the chalcone derivative. It describes the distribution of charges in the molecular orbital's several subshells (core, valance, Rydberg). Table 8 shows the accumulation of natural charges on individual atoms of the title molecule. The Mulliken atomic charge calculation plays a significant role in quantum chemical calculations of molecular systems. The dipole moment, polarizability, electronic structure, and other molecular properties of the system are all affected by atomic charge. In Fig.7, atoms were coloured according to their Mulliken charges, and a graphical representation was displayed.

Atoms	Mulliken Charges	Atoms	Mulliken Charges	Atoms	Mulliken Charges
C_1	0.392829	H_{13}	0.220595	C_{25}	-0.090027
C_2	0.212872	C_{14}	0.508612	C_{26}	-0.152129
C_3	-0.192027	N_{15}	-0.794911	C_{27}	0.055655
C_4	-0.037183	H_{16}	0.355994	C_{28}	-0.155310
C_5	-0.130909	O_{17}	-0.384455	C_{29}	-0.166850
C_6	-0.114917	C_{18}	0.169208	H_{30}	0.155414
H_7	0.173574	C_{19}	-0.153641	H_{31}	0.152237
H_8	0.164291	H_{20}	0.196551	H_{32}	0.157437
H_9	0.200460	C_{21}	-0.173340	H_{33}	0.163726
O_{10}	-0.497500	H_{22}	0.183777	C_{34}	-0.612695
C_{11}	-0.255711	O_{23}	-0.393198	H_{35}	0.198738
H_{12}	0.234452	C_{24}	0.016589	H_{36}	0.189962
				H_{37}	0.201829

Table 8. Mulliken Atomic Charges at B3LYP/6-311++G(d,p)

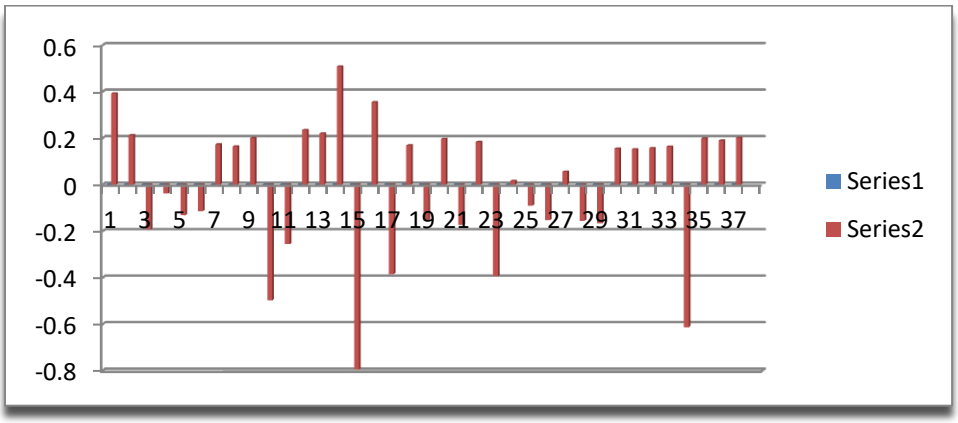

Fig.7.Mulliken Charges and graphical representation at B3LYP/6-311++G(d,p)

Molecular Electrostatic Potential (MEP)

The electrostatic potential created in the area around a particle by its cores and electrons (considered as static conveyances of charge) is a very useful attribute for breaking down and anticipating subatomic responsive conduct.

The potential has shown to be particularly useful as a marker of the destinations or locations of a particle to which an approaching electrophile and nucleophile are initially pulled in. The atomic electrostatic potential (MEP) is related to the electronic thickness and is a very useful descriptor for determining electrophilic and nucleophilic assault sites, as well as hydrogen-holding connections. Figure 8 shows the sensitive locations for electrophilic and nucleophilic assault on HMHP-I. The responsive destinations can be located via MEP investigation and various shading codes. The MEP realistic's red tone depicts an Electron-rich site, which is a negative location with Electrophilic reactivity. In the MEP realistic, the blue tone depicts an Electron-lacking site, which is a positive location indicating Nucleophilic reactivity. In addition, the Green tone in the MEP accurately depicts a neutral, zero electrostatic potential region with Hydrogen-holding connections.

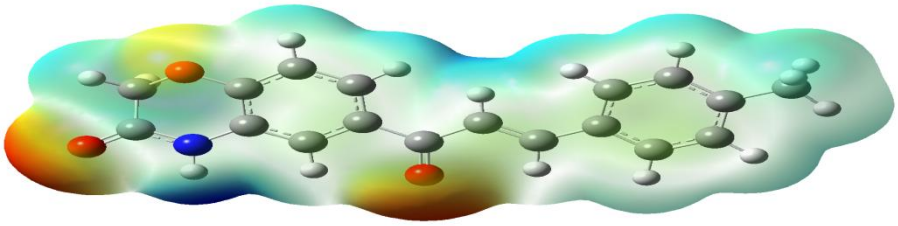

Fig.8. MEP Reactive Sites Calculated at B3LYP/6-311++G(d,p)

Hirshfeld surface analysis

“The Hirshfeld surface has shown to be a useful tool for visually examining intermolecular interactions” [16]. “Molecule Hirshfeld surfaces are created by dividing crystal space into regions where the electron distribution of a sum of spherical atoms for the molecule (promolecule) dominates the corresponding sum over the crystal (procrystal). The Hirshfeld surface is the 0.5 isosurface for the normalised weighted electron density (or weight function w(r) = 0.5), which is defined as the ratio of the promolecule's electron density to that of the procrystal's electron density” [17, 18].

$$w(r) = \frac{\sum_{a\varepsilon\ molecule}[\rho_a(r)]}{\sum_{a\varepsilon\ crystal}[\rho_a(r)]} = \frac{\rho_{promolecule}(r)}{\rho_{procrystal}(r)} \qquad \text{----------(1)}$$

Crystal Explorer 3.0 [19] is used to create Hirshfeld surfaces and their associated fingerprint plots. The Crystal Explorer programme takes a single-crystal X-ray diffraction

Crystallographic Information File (.cif) file as input. For a given crystal structure and set of spherical atomic electron densities, the Hirshfeld surface is unique. Two distances are defined for each point on the 3D Hirshfeld surface: the distance between the Hirshfeld surface and the nearest nucleus inside the surface di and the distance between the surface and the nearest nucleus outside the surface de. Then there's dnorm, which is a normalised contact distance defined in terms of the atoms' di, de, and vander Waals (vdW) radii [20, 21].

$$d_{norm} = \frac{d_i - r_i^{vdw}}{r_i^{vdw}} + \frac{d_e - r_e^{vdw}}{r_e^{vdw}} \qquad \text{----------(2)}$$

By mapping dnorm across the Hirshfeld surface, the-Fig. 9 is generated. It also shows intermolecular interactions with the molecules around it. The surfaces are transparent to allow viewing of the functional groups' orientation and conformation within the surface. Green dotted lines represent the C–H•••O hydrogen bonds. The dnorm values [22, 30, 31] are mapped over the Hirshfeld surface using a red–white–blue colour scheme, with red representing closer contacts with a negative dnorm value, white representing the distance of contacts exactly comparable to the Van der Waals separation with a dnorm value of zero, and blue representing longer contacts with a positive dnorm value. The big circular deep red coloured depressions on dnorm surfaces suggest hydrogen-bonding connections, whereas other spots show H–H contacts.

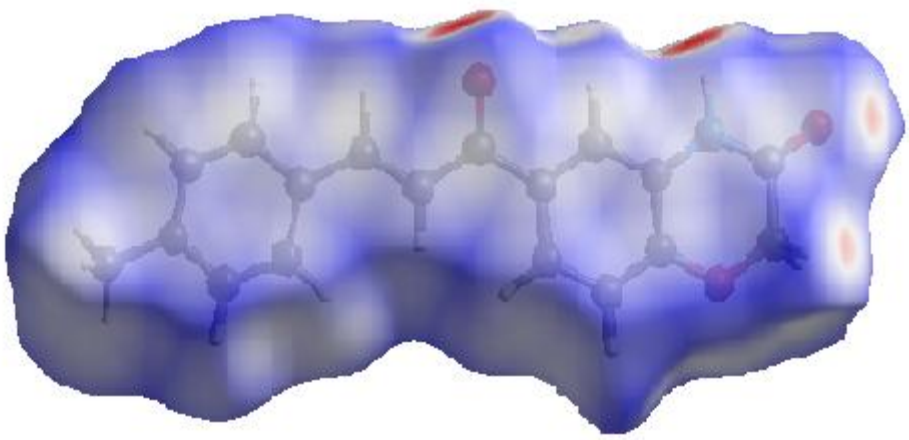

Fig.9- Hirshfeld surface of compound 6TABO

The nature and kind of intermolecular interactions experienced by the molecules in the crystal are quantified by the 2-D fingerprint plots. It compares the distance (di) between the closest atom inside the surface and the distance (de) between the nearest atom outside the surface. “The two-dimensional fingerprint plots are made by binning (di, de) pairings and

colouring each bin according to the fraction of surface points in that bin, ranging from blue (few points) to green (moderate fraction) to red (large fraction) (many points). The whole fingerprint outline is presented in grey colour" [23-31].

Different interactions can be distinguished from one another in this study, which would normally overlap in full fingerprint plots. Figure 10 shows the compound's 2-D fingerprint plots for all main intermolecular interactions, along with their % contribution to the total Hirshfeld surface area for the molecule. Fig. 10a shows the 2D fingerprint plot for all intermolecular interactions. The H•••H interactions, which are reflected in the centre of scattered points and cover the majority of the region in the 2-D fingerprint plots shown in Fig. 10b, contribute the most to the total Hirshfeld surfaces, accounting for 47.31 percent. In the 2D fingerprint plots, the H•••O hydrogen bonding intermolecular interactions contribute 11.51 percent to the total Hirshfeld surfaces, as seen in Fig. 10c. In the 2D fingerprint plots, the C•••C (Fig.10d.) and C•••H interactions (Fig.10e.) contribute 14.2% and 5.8% of the total Hirshfeld surfaces, respectively. As a result, both Hirshfeld surfaces and fingerprint plots make it easier to compare intermolecular interactions in the construction of supramolecular motifs in the crystal structure.

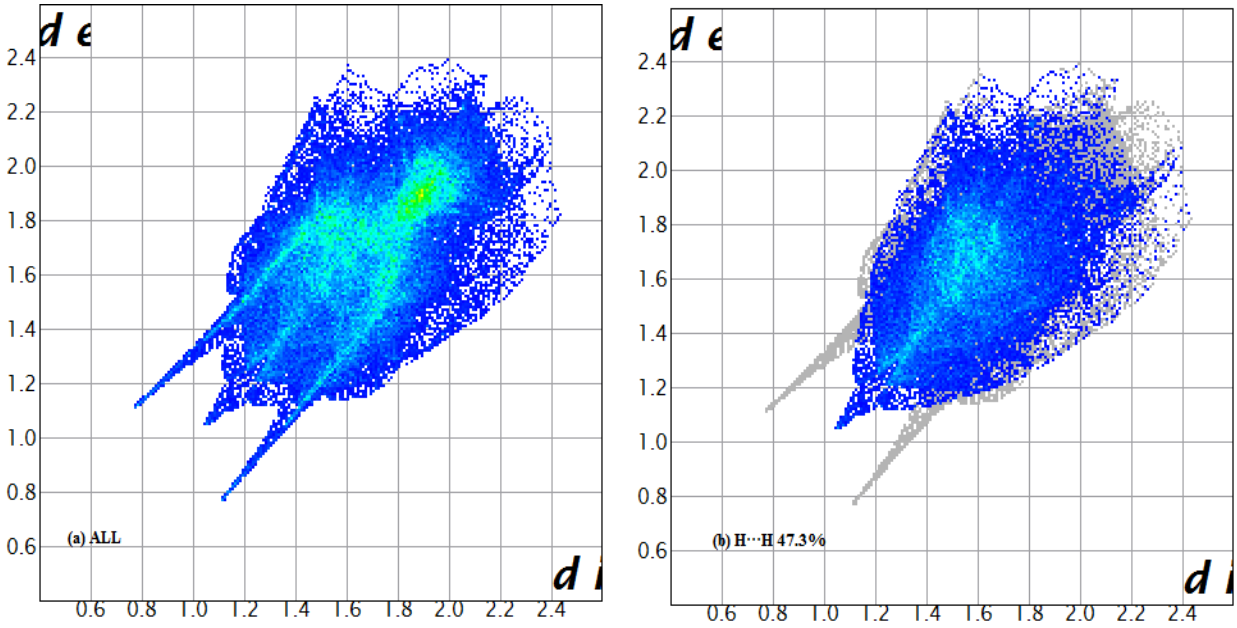

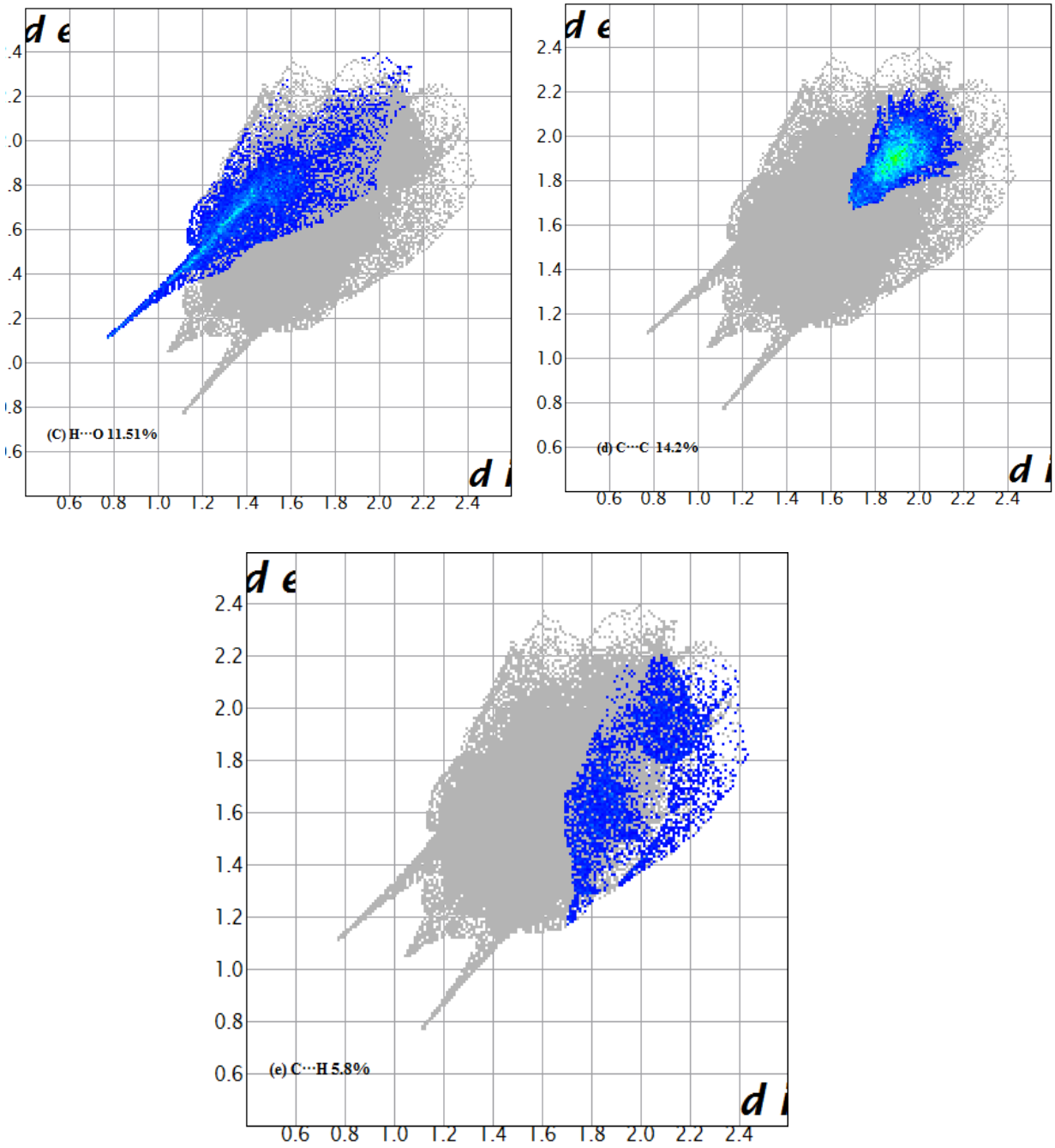

Fig. 10. Fingerprint plots of the compound where di and de are in Å

(a) The total contribution from all the interactions (b) H···H, (c) H···O, (d) C···C, (e) C···H, showing the percentage of contacts contributed to the total Hirshfeld surface area for the molecule. Blue color represents a low percentage of contacts and green a moderate percentage of contacts and outline of the full fingerprint is shown in grey.

Conclusion

A new chalcone derivative (E)-6-(3-(p-tolyl)acryloyl)-2H-benzo[b][1,4]oxazin-3(4H)-one [6TABO] has been synthesized using the Claisen–Schmidt condensation reaction method. The structure is confirmed with the help of FT-IR spectra and ^{1}H NMR spectrum. Crystal parameters are determined by single-crystal XRD study. The UV–visible study of MMPP indicates that the crystal is transparent in the entire visible range.

Conflict of Interest

The Authors declare that there is no conflict of interest.

REFERENCES

1. B.P. Bandga, S.A. Patil, B.L. Korbad, S.H. Nile, C.N. Khobragade, Eur. J. Med. Chem. 45,2629–2633 (2010) .
2. N.Sunduru, A. Agarwal, S.B. Katiyar, Nishi, N. Goyal, S. Gupta, P.M.S. Chauhan, Bioorg. Med. Chem. 14, 7706–7715 (2006).
3. Tatsuzaki, K.F. Bastow, K. Nakagawa-Goto, S.Nakamura, H. Itokawa, K.-H. Lee, J. Nat. Prod.69(10), 1445–1449 ,(2006) .
4. J.-M. Yun, M.-H. Kweon, H. Kwon, J.-K.Hwang, H. Mukhtar, Carcinogenesis 27(7), 1454–1464 (2006).
5. V. Calvino, M. Picallo, A.J. Lpoz- Peinado, R.M. Martin-Aranda, C.J.Duran-Valle, Appl. Surface Sci. 252(17), 6071–6074 (2006).
6. J.J. McKinnon, M.A. Spackman, A.S. Mitchell, Novel tools for visualizing and exploring intermolecular interactions in molecular crystals, ActaCryst. Section B 60 (2004) 627-668.
7. M.A. Spackman, D. Jayatilaka, Hirshfeld surface analysis, CrystEngComm 11 (2009)19-32.
8. M.A. Spackman, J.J. McKinnon, Fingerprinting Intermolecular Interactions in Molecular Crystals, CrystEngComm 4 (2002) 378-392.
9. K.S. Dhami and J.B. Stothers, Can. J. Chem., **1963, 43, 479**
10. K.S. Dhami and J.B. Stothers, Can. J. Chem., **1965,**43,510.
11. P.C Leuterbur, J .Am. Chem. Soc ., **1961,**83,1846.
12. Vincent Crasta, V. Ravindrachary, R.F. Bhajantri, Richard Gonsalves, J. Cryst. Growth 267 (2004) 129.
13. S. Gunasekaran, R. A. Balaji, S. Kumeresan, G. Anand and S. Srinivasan, Experimental and theoretical investigations of spectroscopic properties of N-acetyl-5-methoxytryptamine, Can. J. Anal. Sci. Spectrosc 53, 149 (2008).
14. S. S. Amiri, S. Makarem, H. Ahmar, and S. Ashenagar, Theoretical studies and spectroscopic
15. characterization of novel 4-methyl-5-((5-phenyl- 1, 3, 4-oxadiazol-2-yl) thio) benzene-1, 2-diol,J.Mol. Struct. 1119, 18 (2016).

16. M. Khalid, M. Ali, M. Aslam, S. H. Sumrra, M.U. Khan, N. Raza, N. Kumar, and M. Imran, Frontier molecular, Natural bond orbital, UV-Vis spectral study, Solvent influence on geometric parameters, Vibrational frequencies andsolvation energies of 8-Hydroxyquinoline, Int. J.Pharma. Sci. and Res., 8, 457 (2017).
17. G.R. Meredith, J. VanDusen, D.J. Williams, Optical and nonlinear optical characterization of molecularly doped thermotropic liquid crystalline polymers, Macromolecules 15 (1982) 1385–1389.
18. J.J. McKinnon, M.A. Spackman, A.S. Mitchell, Novel tools for visualizing and exploring intermolecular interactions in molecular crystals, ActaCryst. Section B 60 (2004) 627-668.
19. M.A. Spackman, D. Jayatilaka, Hirshfeld surface analysis, CrystEngComm 11 (2009)19-32.
20. M.A. Spackman, J.J. McKinnon, Fingerprinting Intermolecular Interactions in Molecular Crystals, CrystEngComm 4 (2002) 378-392.
21. L. Vivien, N. Izard, D. Riehl, F. Hache, E. Anglaret, Optical Limiting Properties of Suspensions of Single-Wall Carbon Nanotubes, AIP Conf Proc. 685 (2003) 559-563.
22. Brian S. Furniss, Antony J. Hannaford, Peter W.G. Smith and Austin R. Tatchell, Vogel's Textbook of Practical Organic Chemistry, Fifth Edition, Longman Scientific& Technical, UK, 1989.
23. J. C. Brice, The Growth of Crystals from Liquids, North-Holland Publishing Company, London, 1973.
24. J.P. Abraham, D. Sajan, V. Shettigar, S.M. Dharmaprakash, I. Nemec, I. Hubert Joe, V. S. Jayakumar, Efficient π-electron conjugated push-pull nonlinear optical chromophore 1-(4- methoxyphenyl)-3-(3,4-dimethoxyphenyl)-2-propen-1-one: A vibrational spectral study, Journal of Mol. Structure 917 (2009) 27-36.
25. Donald L. Pavia, Gary M. Lampman, George S. Kriz, Introduction to Spectroscopy, 3rd Edition, Thomson Learning, US, 2001.
26. P.S. Kalsi, Spectroscopy of Organic Compounds, 2nd Edition, Wiley Eastern Limited, New Delhi, 1995.
27. G.M. Sheldrick, ActaCryst. A short history of SHELX, A 64 (2008) 112-122.
28. C. Dong, PowderX: Windows-95-based program for powder X-ray diffraction data processing, J. Appl. Crystallogr. 32 (1999) 838-838.
29. M.A. Spackman, P. G. Byrom, A novel definition of a molecule in a crystal, Chem. Phys. Lett. 267 (1997) 215-220.
30. S.K. Wolff, D.J. Grimwood, J.J. McKinnon, M.J. Turner, D. Jayatilaka, M.A. Spackman, Crystal Explorer (Version 3.1), University of Western Australia, 2012.
31. J.J. McKinnon, D. Jayatilaka, M.A. Spackman, Towards quantitative analysis of intermolecular interactions with Hirshfeld surfaces, Chem. Commun. 37 (2007) 3814 – 3816.